Vol. 28 • No. 13 • April 6 • 2016

www.advmat.de

ADVANCED MATERIALS

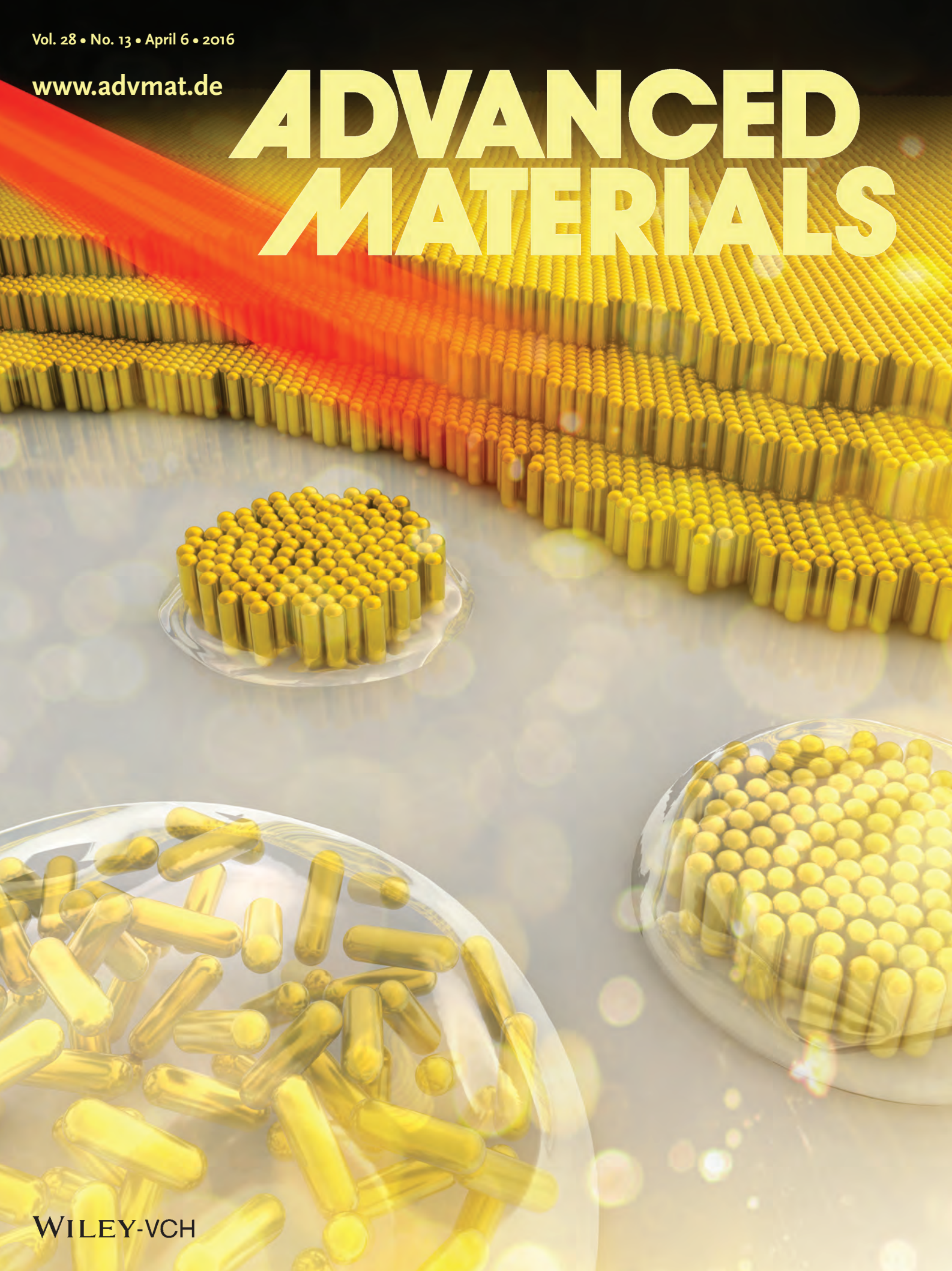

WILEY-VCH

Evaporative Self-Assembly of Gold Nanorods into Macroscopic 3D Plasmonic Superlattice Arrays

Penghui Li, Yong Li, Zhang-Kai Zhou, Siying Tang, Xue-Feng Yu, Shu Xiao, Zhongzhen Wu, Quanlan Xiao, Yuetao Zhao, Huaiyu Wang, and Paul K. Chu**

One of the research foci in the emerging fields of plasmonics[1–3] and metamaterials[4–6] is the self-assembly of nanoparticles[7,8] into macroscale 3D superlattice arrays possessing collective properties. In particular, the self-assembly of nonspherical nanoparticles has become popular because such superstructures can stimulate some anisotropic optical and electrical properties and meet practical needs demanded by optoelectronic devices,[9–12] enhanced spectroscopies,[13–15] and solar cells.[16] Gold nanorods (AuNRs), as a typical anisotropic building block, are suitable self-assembled superstructures because their collective plasmonic properties depend on the local density and orientation.[17,18] Assembled AuNRs have exhibited extremely high electromagnetic fields to yield enhanced optical signals.[19–22] However, the size of current assembled 3D plasmonic superlattices is generally only a few micrometers thereby limiting their use in many macroscopic applications. It is still a big challenge to assemble plasmonic nanoparticles into a macroscopic and homogenous 3D superlattice with millimeter dimensions.

Among the various techniques to fabricate superlattice structures, droplet evaporation has been extensively investigated because of the operability, cost-effectiveness, and wide applicability to various functional nanomaterials.[23–29] However, despite the simple nature, particle deposition from evaporating sessile drops has complex mechanisms and is difficult to control.[30–32] Typically, drying of a droplet containing nonvolatile solutes normally leaves a ring of solute deposited on the surface instead of a uniform distribution and it is the well-known coffee-ring effect which is frequently adopted to pattern solutes on surfaces.[33–35] Nonetheless, it presents a serious obstacle in evaporative self-assembly requiring homogenous particle deposition.[36,37] Recent research has been devoted to overcoming or suppressing the coffee-ring effect by regulating the shape and stickiness of particles,[38–40] type, charge, and concentration of surfactants,[41–43] substrate,[44,45] and it has been reported that the coffee-ring effect can be mitigated in other film processing methods like doctor blading or drag coating.[46,47] However, control of the coffee-ring effect in evaporative self-assembly is difficult because many factors affect particle deposition, for instance, particle–particle interaction, particle–suspension interaction, and droplet–substrate interaction.[48,49] A strategy to totally suppress or even reverse the coffee-ring effect is highly desirable in order to accomplish homogenous self-assembly of nanoparticles into a macroscopic structure.

Herein, a simple and efficient evaporative self-assembly method is presented to control particle deposition against coffee rings by regulating the surface properties of the AuNRs and substrates. By completely reversing the coffee-ring effect, macroscopic 3D plasmonic superlattice arrays composed of dense, regular, and nearly vertically aligned AuNRs are fabricated. The fabrication mechanism, structure, and Raman enhancement are investigated systematically.

As building blocks for evaporative self-assembly, the AuNRs (58.0 ± 6.0 nm length; 16.3 ± 2.0 nm width) are prepared by the well-known seed-mediated method, in which hexadecyltrimethylammonium bromide (CTAB) is used as the capping ligand.[50] The surface of the AuNRs is capped by a bilayer of partially interdigitated CTAB molecules thus producing a strong positive charge. This yields CTAB-coated AuNRs (named as CTAB-AuNRs) with high stability against aggregation. However, the associated repulsive force hinders close packing of the rods during self-assembly and so it is crucial to further functionalize the CTAB-AuNRs to facilitate self-assembly. In this context, we implement the exchange between the capping ligand CTAB and (11-mercaptoundecyl)hexa(ethylene glycol) (MUDOL), a commercially available amphiphilic PEGylated alkanethiolate ligand bearing a thiol moiety (**Figure 1**a). After gentle stirring for 24 h, MUDOL molecules gradually displace the CTAB molecules on the surface of the AuNRs because of the stronger ligand bond between Au and S.

After the exchange between CTAB and MUDOL, the surface properties of the AuNRs are determined by Fourier transform

Dr. P. Li, Y. Li, S. Tang, Prof. X.-F. Yu, Dr. Q. Xiao, Dr. Y. Zhao, Prof. H. Wang
Institute of Biomedicine and Biotechnology
Shenzhen Institutes of Advanced Technology
Chinese Academy of Sciences
Shenzhen 518055, P. R. China
E-mail: xf.yu@siat.ac.cn

Dr. P. Li, Prof. P. K. Chu
Department of Physics and Materials Science
City University of Hong Kong
Tat Chee Avenue
Kowloon, Hong Kong, P. R. China
E-mail: paul.chu@cityu.edu.hk

Prof. Z.-K. Zhou
State Key Laboratory of Optoelectronic Materials and Technologies
School of Physics and Engineering
Sun Yat-sen (Zhongshan) University
Guangzhou 510275, P. R. China

S. Xiao, Prof. Z. Wu
School of Advanced Materials
Peking University Shenzhen Graduate School
Shenzhen 518055, P. R. China

DOI: 10.1002/adma.201505617

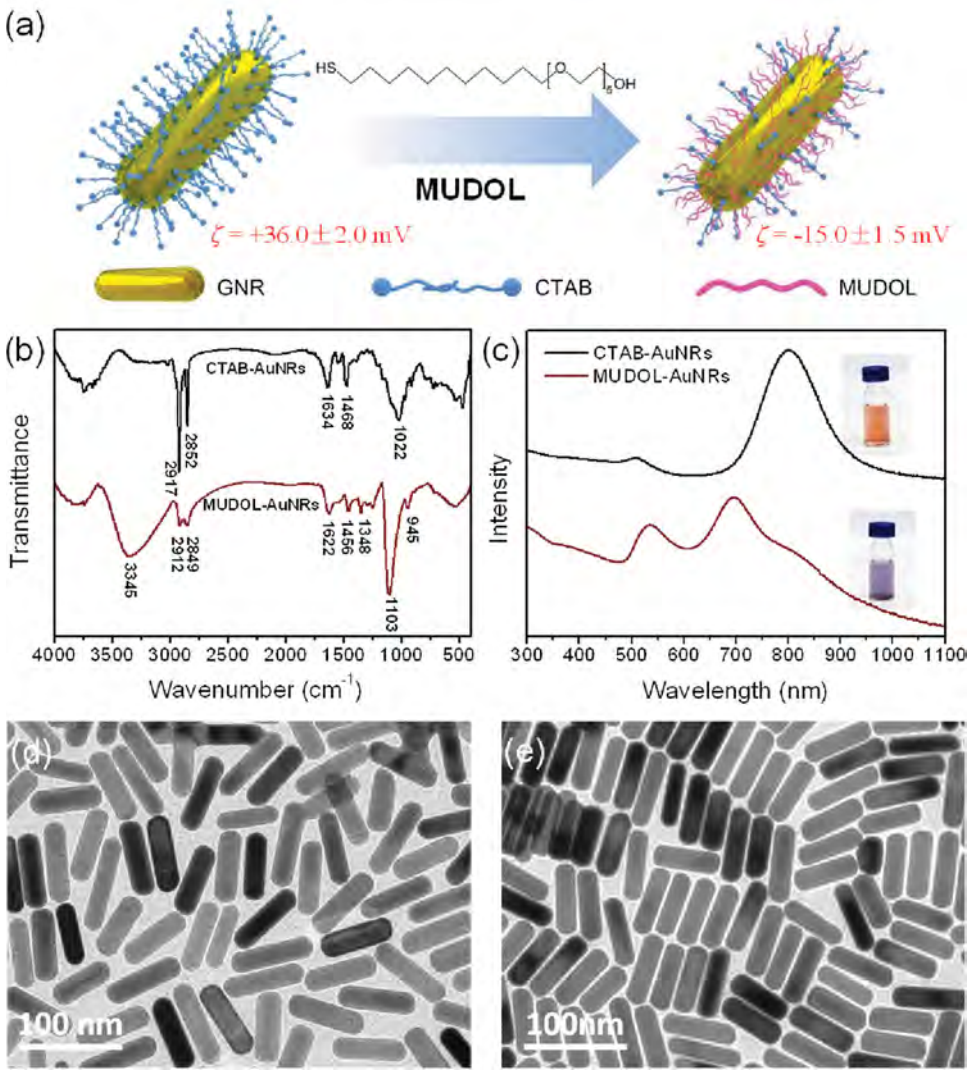

Figure 1. a) Schematic illustration of the surface ligand exchange between CTAB-AuNRs and MUDOL molecules. b) FTIR spectra of CTAB-AuNRs and MUDOL-AuNRs. c) Absorption spectra of CTAB-AuNRs and MUDOL-AuNRs aqueous solution with respective photos in the inset. d,e) TEM images of CTAB-AuNRs and MUDOL-AuNRs.

infrared (FTIR) spectroscopy (Figure 1b). After the exchange, the broad band at 1022 cm^{-1} considered to the C–N^+ stretching disappears whereas a new intense band at 1100 cm^{-1} arising from C–O–C stretching in ethylene glycol moieties of MUDOL-coated AuNRs (named as MUDOL-AuNRs) is observed.[21] The characteristic peaks of –OH in the MUDOL molecule manifest as a broad peak around 3345 cm^{-1}. FTIR spectroscopy suggests that CTAB is exchanged with MUDOL and the latter molecules are densely packed on the nanorod surface. The high positive surface charge of CTAB-AuNRs ($\zeta = +36.0 \pm 2.0$ mV) is gradually lowered to becoming slightly negative MUDOL-AuNRs ($\zeta = -15.0 \pm 1.5$ mV). These results clearly demonstrate successful exchange between CTAB and MUDOL on the AuNRs.

Figure 1c shows the absorption spectra of the CTAB-AuNRs and MUDOL-AuNRs. After the exchange, the longitudinal surface plasmon resonance (SPR) band peak of the AuNRs blueshifts from 800 to 695 nm and obvious redshift and intensity enhancement can be observed from the transverse SPR band. Correspondingly, the color of the AuNRs solution changes from pink to purple. The variations in the SPR bands suggest side-to-side assembly of the MUDOL-AuNRs and the decreased aspect ratio and increased diameter produce the blueshifted longitudinal SPR band and redshifted transverse SPR band, respectively. The MUDOL induced side-to-side assembly is confirmed by the transmission electron microscopy (TEM) images of the CTAB-AuNRs and MUDOL-AuNRs as shown in Figure 1d,e, respectively.

In order to study the deposition and assembly behavior of the AuNRs during droplet evaporation, droplets of the CTAB-AuNRs and MUDOL-AuNRs are used as the colloidal suspensions and two kinds of substrates, including Si wafer and Si with SiO_2 surface layer (Si/SiO_2), are used as well. The Si wafers with the <100> orientation are purchased and Si/SiO_2 wafers with 300 nm surface oxide are prepared by thermal oxidation of the Si wafers. The distinct surface chemical structures

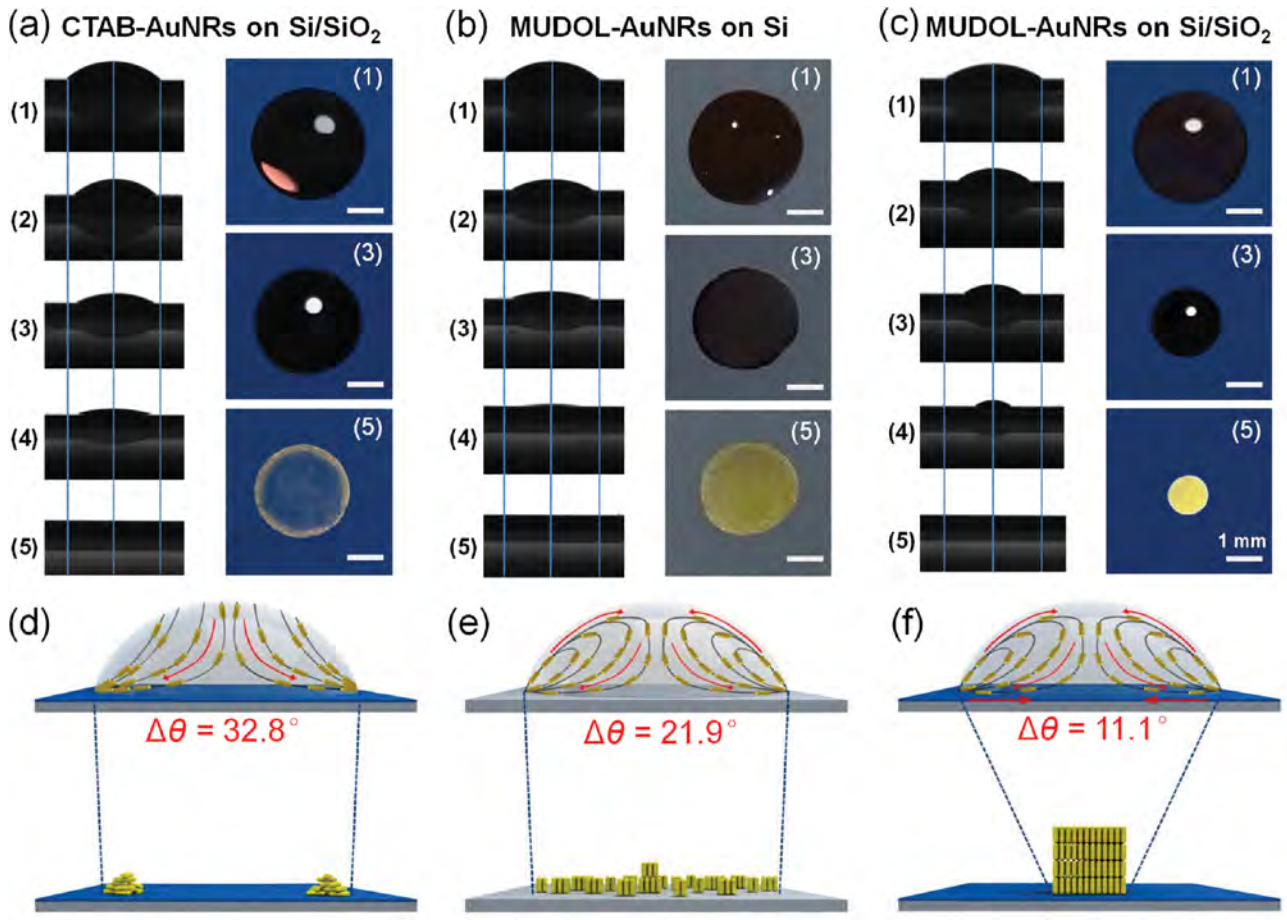

Figure 2. a–c) Side (left) and top (right) views and d–f) schematic illustration of different AuNRs deposition behavior during evaporation: a,d) CTAB-AuNRs on Si/SiO_2, b,e) MUDOL-AuNRs on Si, and c,f) MUDOL-AuNRs on Si/SiO_2.

of the two substrates are presented in the X-ray photoelectron spectroscopy (XPS) spectra in Figure S1 (Supporting Information), especially the signals at 99.1 and 103.0 eV representing Si and SiO_2 in the high-resolution Si 2p spectra. The atomic force microscopy (AFM) examinations demonstrate that the two wafers have the similar surface roughness (Figure S1, Supporting Information). The use of the substrates with similar surface roughness minimizes the effect of surface roughness on the deposition and assembly behavior. The droplets are allowed to evaporate on a substrate at a humidity of 85% ± 5% at room temperature. The volume of the suspension is 4.0 µL and the concentration of the AuNRs is 15.0×10^{-9} M. The evaporation process is monitored from the side and the top every 18 h using a contact angle goniometer and digital camera, respectively.

As shown in **Figure 2**, three different kinds of AuNRs patterns are obtained due to the different deposition behavior influenced by the suspension and substrate. When the CTAB-AuNRs suspension is evaporated on the Si (Figure S2, Supporting Information) or Si/SiO_2 (Figure 2a) substrate, the base diameter of the droplet only decreases in the early stage of evaporation and becomes almost the same afterward. After complete drying of the droplet, the vast majority of the CTAB-AuNRs deposited near the out ring form a coffee-ring like pattern with a diameter of around 2.5 mm slightly smaller than the initial droplet base diameter. When the MUDOL-AuNRs suspension is evaporated on the Si substrate, they show relatively homogenous deposition resulting in a disk-like pattern with a diameter of about 2.6 mm. Interestingly, the MUDOL-AuNRs suspension on the Si/SiO_2 substrate shows a completely different evaporation process (Figure 2c). The base diameter of the sessile droplet keeps decreasing until complete drying of the droplet. A smaller and thicker concentrated disk-like pattern with a diameter of only 1.2 mm is obtained finally and furthermore, the visible metallic luster of the pattern suggests ordered close-packing of the AuNRs.

The mechanism of the formation of the three kinds of AuNRs patterns is analyzed (see Figure 2d–f). The CTAB-AuNRs produce a coffee-ring like pattern due to the well-known coffee-ring effect involving capillary edgeward flow and pinned contact line during evaporation. Contact line pinning of the drying droplet on the surface leads to water flow from the interior to replenish the water evaporating from the edge (see Figure 2d). The resulting edgeward flow carries nearly all the AuNRs toward the edge and deposits them in the vicinity of the contact line to form a ring-like pattern. In contrast, alteration of the surfactant type in the MUDOL-AuNRs suspension induces the Marangoni effect.

The radial outward flow brings the solutes to the contact line thus increasing the local concentration and decreasing the surface tension close to the drop edge. The gradient in surface tension along the liquid-gas interface induces a Marangoni flow from the edge to the apex of the drop (Figure 2e,f). This surface flow is expected to push the AuNRs away from the stagnation contact line causing them redistribute back to the central region consequently suppressing the coffee-ring effect.[42]

Compared to MUDOL-AuNRs on Si, MUDOL-AuNRs on Si/SiO_2 produce a significantly concentrated pattern which can account for the significant receding of the contact line. Pinning or receding of the contact line is associated with contact angle hysteresis ($\Delta\theta$), which is generally expressed in terms of the difference between the advancing and receding contact angles ($\Delta\theta = \theta_a - \theta_r$).[51] Contact-angle hysteresis is accompanied by pinning of the contact line as the drop is withdrawn. Because of contact line pinning, the contact angle decreases with decreasing droplet volume and eventually, the contact angle reaches θ_r and the contact line begins to withdraw. Thus, the extent of contact-angle hysteresis of the liquid on the substrate affects the extent of the contact line receding.[41] The contact angle hysteresis of the two liquids CTAB-AuNRs and MUDOL-AuNRs on Si and Si/SiO_2 is evaluated by measuring the advancing and receding contact angles (see Table S1, Supporting Information). $\Delta\theta$ of CTAB-AuNRs on Si or Si/SiO_2 is as large as 32.8° and 32.4°, respectively, whereas $\Delta\theta$ of MUDOL-AuNRs on Si is 21.9°. Noticeably, $\Delta\theta$ of MUDOL-AuNRs on Si/SiO_2 is only 11.1° which is the smallest one demonstrating that receding of the contact line is most significant. The significant contact angle hysteresis of the MUDOL-AuNRs suspension on the Si/SiO_2 substrate leads to receding of the contact line and hence, the coffee-ring effect is totally reversed other than suppressed. It can be concluded that the Marangoni flow and contact line receding can efficiently control the final pattern of AuNRs on the substrate. The method presented here provides an efficient strategy to reverse the coffee-ring effect during evaporation of nanoparticles and makes homogenous deposition and close-packing of AuNRs possible.

The morphology and structure of the three kinds of AuNRs patterns are characterized at different scales by confocal laser scattering microscopy and scanning electron microscopy (SEM). **Figure 3**a clearly shows the 3D morphology of a partial area of the coffee-ring like pattern formed by the CTAB-AuNRs on the Si/SiO_2 substrate. The SEM images in Figure 3b,c reveal horizontal self-assembled AuNRs at the out rim of the coffee-ring with few randomly scattered AuNRs in the middle area forming a coffee-ring like array of AuNRs (named as coffee-ring array). In contrast, for the MUDOL-AuNRs on the Si substrate, a relatively flat surface is obtained due to suppression of the coffee-ring effect (Figure 3d). The SEM images in Figure 3e,f clearly show self-assembly of the AuNRs forming an array with few layers of the AuNRs (named as few-layer array). However, the distribution of the self-assembled AuNRs is far from homogeneous. The pattern has cracks and blank gaps can be observed from the array.

Interesting results are obtained from the self-assembly of the MUDOL-AuNRs on the Si/SiO_2 substrate. The pattern

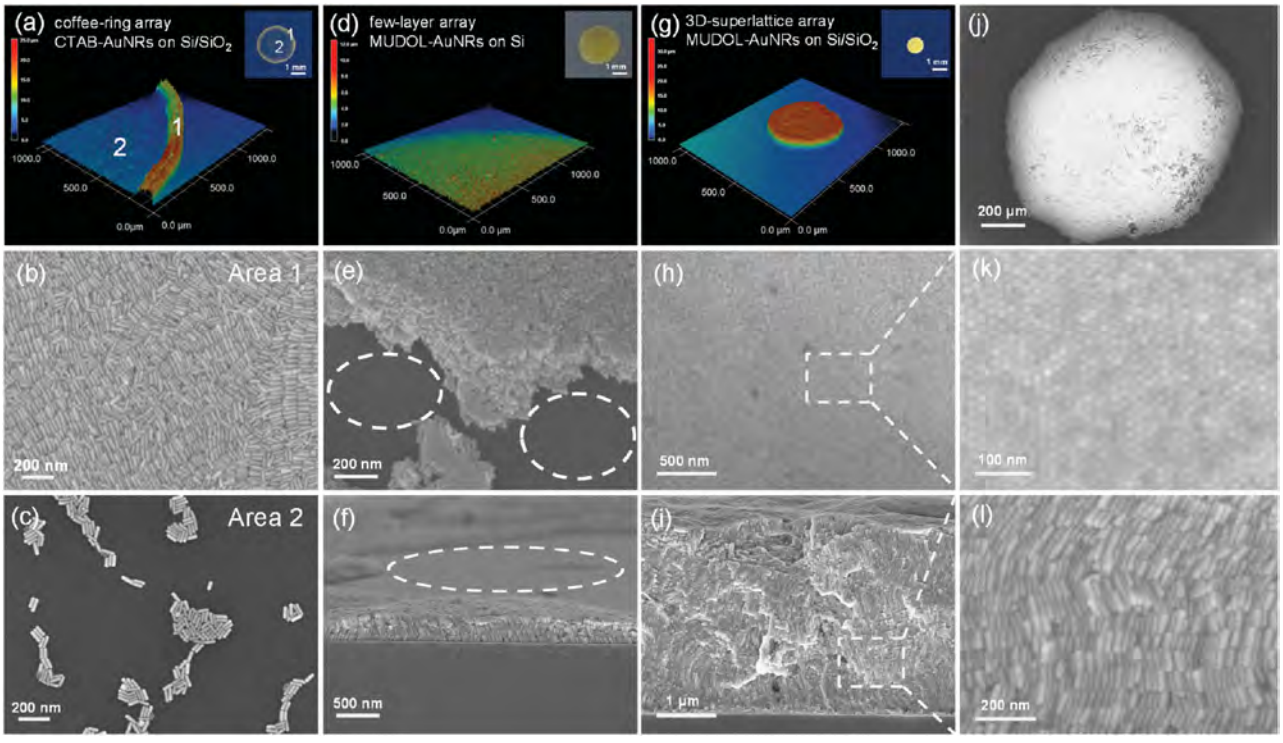

Figure 3. Confocal laser scattering microscopic 3D images with inset photographs and SEM images of: a–c) coffee-ring array formed by CTAB-AuNRs on the Si/SiO_2 substrate, d–f) few-layer array formed by MUDOL-AuNRs on Si substrate, and g–l) 3D-superlattice array formed by MUDOL-AuNRs on Si/SiO_2 substrate.

possesses a 3D disk-like morphology as shown by Figure 3g. The typical SEM image of the entire array in Figure 3j indicates dense self-assembly of the AuNRs with a millimeter scale. The top-view SEM images in Figure 3h,k show that the AuNRs are completely vertically ordered forming a superlattice structure. The cross-sectional SEM images in Figure 3i,l confirm that the ordered AuNRs assembly structure consists of tens of layers of densely packed standing AuNRs. The figures reveal successful self-assembly of the AuNRs into a homogeneous macroscopic 3D superlattice array (named as 3D-superlattice array) in which all the AuNRs are dense, regular, and nearly vertically aligned with respect to the surface of the substrate. All the results demonstrate that the synergism of AuNRs surface chemistry, surfactant, and substrate can totally reverse the coffee-ring effect and result in the formation of such assembled superlattice structure. Even if the CTAB-AuNRs with added MUDOL (without the ligand exchange protocol) are evaporated on the Si/SiO_2 substrate, such perfect ordered assembly of AuNRs cannot be achieved (see details in Figure S3 in the Supporting Information).

After optimization of the evaporative self-assembly of AuNRs, the plasmonic properties of the 3D-superlattice array are determined in surface-enhanced Raman scattering (SERS). The coffee-ring array and few-layer array are employed as the control. SERS is performed on a commercial Raman spectrometer with 633 nm excitation. Malachite green (MG), a typical banned fish pesticide is selected as a model analyte for SERS detection. Owing to the high SERS activity of the assembled AuNRs, the spectra of the three kinds of arrays clearly show the characteristic Raman peaks of MG; however, their SERS sensitivity and uniformity are quite different. For the coffee-ring array (see Figure S4, Supporting Information), the strong SERS single can be found from the outer rim area of the coffee-ring and it is over two orders of magnitude higher than that from the middle area. The results demonstrate that the uniformity of the SERS signals is unsatisfactory according to the strong heterogeneous distribution of the AuNRs in the coffee-ring array.

Since both the few-layer array and 3D-superlattice array have the similar disk-like pattern, their SERS performance is compared directly. The typical SERS spectra in **Figure 4**a,c show that the SERS signal from the 3D-superlattice array is over ten times that of the few-layer array with the same MG concentration. A 70 μm × 70 μm area in each array is then mapped by point-by-point scanning with a step size of 5 μm (15 × 15 spots each) during laser excitation. The average signal intensity (I_{ave}) at 1615 cm^{-1} from the 225 spots is measured and the relative standard deviation (RSD) of these SERS intensities is calculated (see Figure 4,d). The average signal intensity of the test area of the 3D-superlattice array is about 31043 counts with an RSD of only 7.2%, while few-layer array has an average signal intensity of only 3073 counts with an RSD of as large as 83.4%. The big differences indicate not only much higher SERS sensitivity but also substantially better signal reproducibility from the 3D-superlattice array. The poor uniformity of the few-layer array is due to the loose dispersion of the AuNRs with blank gaps in between (see Figure 3e,f). Among the three kinds of arrays, the best SERS performance observed from the 3D-superlattice array is ascribed to the homogenous, close-packed, and ordered superlattice structure of vertically aligned AuNRs. To further understand the physical mechanism responsible for the observed SERS response, the electric field intensity enhancement of the AuNRs array is investigated by the finite-difference time-domain (FDTD) method (see Figure S5 for details, Supporting Information).

The potential of the 3D-superlattice array as an SERS substrate for ultrasensitive detection of MG is studied. Figure 4e depicts the SERS spectra of MG for different concentrations from 1.0×10^{-6} to 1.0×10^{-10} M. As a result of the excellent SERS activity, the spectra clearly show the characteristic Raman peaks of MG even at a concentration down to 1.0×10^{-10} M, indicating that the detection limit is lower than the technique performance limit (2.0 μg L^{-1}) for MG required by the European Commission and the US Food and Drug Administration. These 3D-superlattice arrays are thus sensitive enough to detect MG in practice.

To further assess the reproducibility of the 3D-superlattice arrays as SERS substrates, a thorough statistical analysis is undertaken to quantify the variations in the SERS signal intensity from different locations on one array (spot-to-spot variation) and between different arrays (array-to-array variation). Figure 4f shows the spot-to-spot variation distribution of the SERS intensity of the 1615 cm^{-1} peak of MG from 15 randomly selected spots along one diameter of a 3D-superlattice array. The RSD is 8.0% which is slightly larger than 7.2% derived from the spots in a 70 μm × 70 μm area (Figure 4b) confirming high reproducibility on a macroscopic scale. To evaluate the array-to-array SERS reproducibility, 5 × 5 3D-superlattice arrays are prepared on the Si/SiO_2 wafer (see Figure 4g) and Raman spectra are acquired one randomly chosen spot on each array (see Figure 4h). The RSD calculated from 25 different substrates is 10.5% indicating good array-to-array reproducibility. These results demonstrate the feasibility of the evaporative self-assembly method in batch production of the 3D-superlattice arrays with good reliability and reproducibility.

In conclusion, we have demonstrated that by regulating the AuNRs surface chemistry, surfactant, and substrate, the coffee-ring effect can be completely reversed and consequently, homogeneous deposition is achieved based on the combined effects of Marangoni flow and contact line receding. Based on this mechanism, millimeter-scale 3D superlattice arrays composed of dense, regular, and vertically aligned AuNRs have been fabricated and demonstrated excellent SERS sensitivity and reproducibility. Compared to previously reported superlattice arrays based on various plasmonic nanoparticles, we have for the first time prepared homogenous 3D-superlattice arrays on the millimeter scale. Such 3D organization of the AuNRs into macroscopic superlattices results in excellent plasmonic substrates suitable for macroscopic sensing applications. With the high reproducibility and operability of the droplet evaporation method, this strategy can be readily extended to the self-assembly of various plasmonic nanoparticles into macroscopic 3D-superlattice arrays and bridge the gap between nanoscale materials and macroscopic applications.

Supporting Information

Supporting Information is available from the Wiley Online Library or from the author.

ADVANCED MATERIALS
www.advmat.de

www.MaterialsViews.com

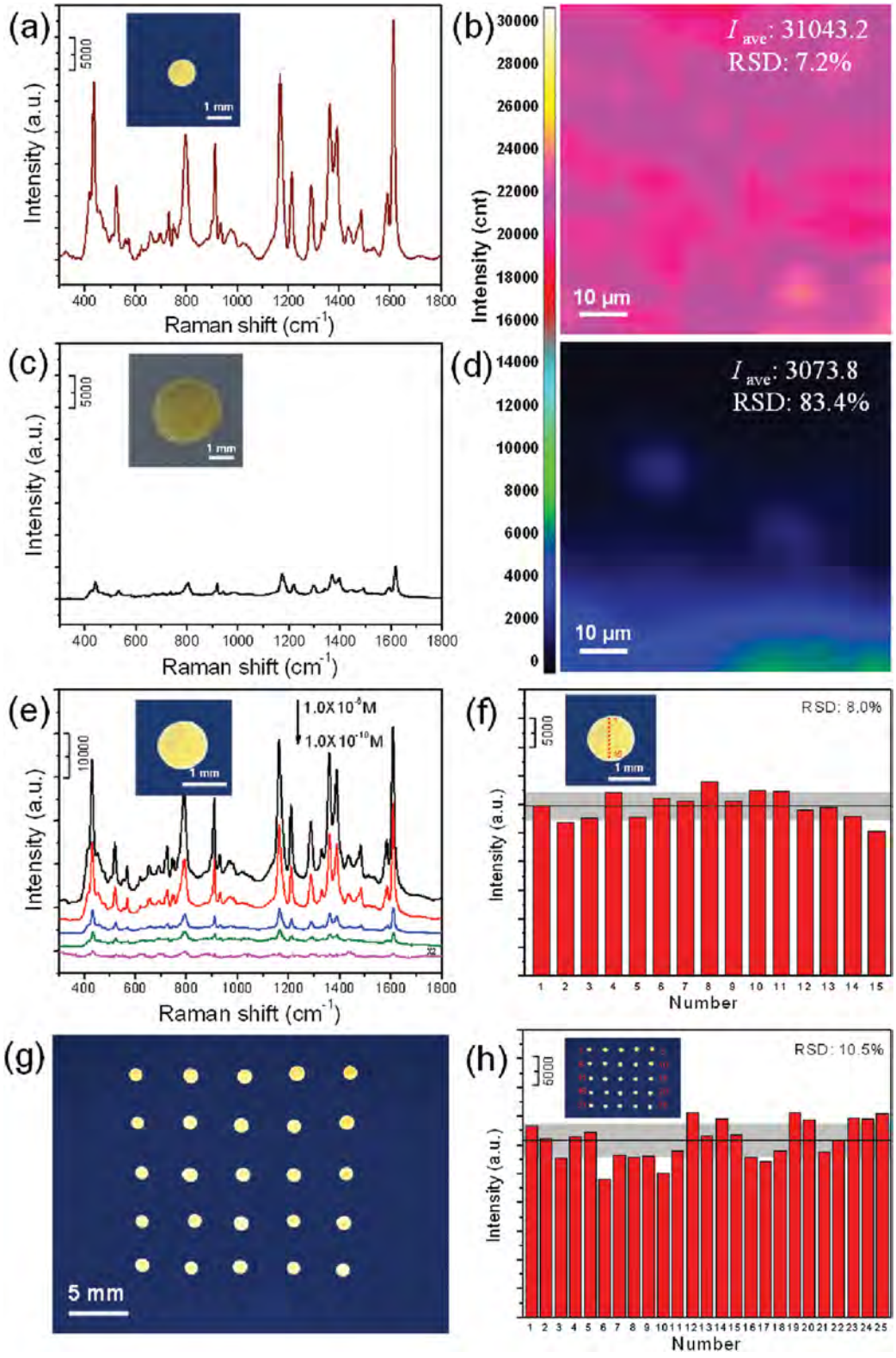

Figure 4. a–d) Typical SERS spectra (λ_{ex} = 633 nm) and SERS intensity maps at 1615 cm^{-1} of MG (1.0×10^{-5} M) on 3D-superlattice array a,b) and few-layer array c,d) formed with MUDOL-AuNRs on Si/SiO_2 and Si, respectively. A 70 μm × 70 μm area in each array is mapped by point-by-point scanning mode using a step size of 5 μm (15 × 15 spots each) upon laser excitation. e) SERS spectra of MG on 3D-superlattice array after treatment with MG solutions with different concentrations. f) Histogram for the peak SERS intensity at 1615 cm^{-1} of MG acquired from 15 different spots on a 3D-superlattice array along the diameter. g) Photograph of a Si/SiO_2 wafer containing 5 × 5 3D-superlattice arrays. h) Histogram of the peak SERS intensity at 1615 cm^{-1} of MG acquired from 25 different 3D-superlattice arrays.

Acknowledgements

P.L. and Y.L. contributed equally to this work. The authors gratefully acknowledge financial support from the National Natural Science Foundation of China (Grant No. 51372175), Science and Technology Key Project of Shenzhen (Grant No. JCYJ20140417113430608), and Guangdong Natural Science Foundation Doctoral Project (Grant No. 2015A030310210).

Received: November 13, 2015
Revised: December 15, 2015
Published online: January 29, 2016

[1] A. Tao, P. Sinsermsuksakul, P. Yang, *Nat. Nanotechnol.* **2007**, *2*, 435.
[2] J. A. Fan, C. Wu, K. Bao, J. Bao, R. Bardhan, N. J. Halas, V. N. Manoharan, P. Nordlander, G. Shvets, F. Capasso, *Science* **2010**, *328*, 1135.
[3] H. Nakanishi, K. J. M. Bishop, B. Kowalczyk, A. Nitzan, E. A. Weiss, K. V. Tretiakov, M. M. Apodaca, R. Klajn, J. F. Stoddart, B. A. Grzybowski, *Nature* **2009**, *460*, 371.
[4] B. Yoon, W. D. Luedtke, R. N. Barnett, J. Gao, A. Desireddy, B. E. Conn, T. Bigioni, U. Landman, *Nat. Mater.* **2014**, *13*, 807.
[5] W. Lewandowski, M. Fruhnert, J. Mieczkowski, C. Rockstuhl, E. Górecka, *Nat. Commun.* **2015**, *6*, 6590.
[6] R. He, Y.-C. Wang, X. Wang, Z. Wang, G. Liu, W. Zhou, L. Wen, Q. Li, X. Wang, X. Chen, J. Zeng, J. G. Hou, *Nat. Commun.* **2014**, *5*, 4327.
[7] A. Dong, J. Chen, P. M. Vora, J. M. Kikkawa, C. B. Murray, *Nature* **2010**, *466*, 474.
[8] Y. Jiao, D. Han, Y. Ding, X. Zhang, G. Guo, J. Hu, D. Yang, A. Dong, *Nat. Commun.* **2015**, *6*, 6420.
[9] Z. Nie, A. Petukhova, E. Kumacheva, *Nat. Nanotechnol.* **2010**, *5*, 15.
[10] K. Miszta, J. de Graaf, G. Bertoni, D. Dorfs, R. Brescia, S. Marras, L. Ceseracciu, R. Cingolani, R. van Roij, M. Dijkstra, L. Manna, *Nat. Mater.* **2011**, *10*, 872.
[11] M. B. Ross, M. G. Blaber, G. C. Schatz, *Nat. Commun.* **2014**, *5*, 4090.
[12] J. Zhang, C. Cao, X. Xu, C. Liow, S. Li, P. H. Tan, Q. Xiong, *ACS Nano* **2014**, *8*, 3796.
[13] Y. H. Lee, W. Shi, H. K. Lee, R. Jiang, I. Y. Phang, Y. Cui, L. Isa, Y. Yang, J. Wang, S. Li, X. Y. Ling, *Nat. Commun.* **2015**, *6*, 6990.
[14] R. A. Alvarez-Puebla, A. Agarwal, P. Manna, B. P. Khanal, P. Aldeanueva-Potel, E. Carbó-Argibay, N. Pazos-Pérez, L. Vigderman, E. R. Zubarev, N. A. Kotov, L. M. Liz-Marzán, *Proc. Natl. Acad. Sci. USA* **2011**, *108*, 8157.
[15] Q.-Q. Wang, J.-B. Han, D.-L. Guo, S. Xiao, Y.-B. Han, H.-M. Gong, X.-W. Zou, *Nano Lett.* **2007**, *7*, 723.
[16] M. J. Rozin, D. A. Rosen, T. J. Dill, A. R. Tao, *Nat. Commun.* **2015**, *6*, 7325.
[17] P. Zijlstra, J. W. M. Chon, M. Gu, *Nature* **2009**, *459*, 410.
[18] P. Zijlstra, P. M. R. Paulo, M. Orrit, *Nat. Nanotechnol.* **2012**, *7*, 379.
[19] B. Peng, G. Li, D. Li, S. Dodson, Q. Zhang, J. Zhang, Y. H. Lee, H. V. Demir, X. Y. Ling, Q. Xiong, *ACS Nano* **2013**, *7*, 5993.
[20] C. Hamon, S. Novikov, L. Scarabelli, L. Basabe-Desmonts, L. M. Liz-Marzán, *ACS Nano* **2014**, *8*, 10694.
[21] C. Hamon, M. Postic, E. Mazari, T. Bizien, C. Dupuis, P. Even-Hernandez, A. Jimenez, L. Courbin, C. Gosse, F. Artzner, V. Marchi-Artzner, *ACS Nano* **2012**, *6*, 4137.
[22] T. Thai, Y. Zheng, S. H. Ng, S. Mudie, M. Altissimo, U. Bach, *Angew. Chem. Int. Ed.* **2012**, *51*, 8732.
[23] J. J. Shao, W. Lv, Q. H. Yang, *Adv. Mater.* **2014**, *26*, 5586.
[24] Y. Zhong, Z. Wang, R. Zhang, F. Bai, H. Wu, R. Haddad, H. Fan, *ACS Nano* **2014**, *8*, 827.
[25] W. van der Stam, A. P. Gantapara, Q. A. Akkerman, G. Soligno, J. D. Meeldijk, R. van Roij, M. Dijkstra, C. de, M. Donega, *Nano Lett.* **2014**, *14*, 1032.
[26] P. He, B. Xu, P. Wang, H. Liu, X. Wang, *Adv. Mater.* **2014**, *26*, 4339.
[27] N. J. Jeon, J. H. Noh, Y. C. Kim, W. S. Yang, S. Ryu, S. I. Seok, *Nat. Mater.* **2014**, *13*, 897.
[28] M. P. Cecchini, V. A. Turek, J. Paget, A. A. Kornyshev, J. B. Edel, *Nat. Mater.* **2013**, *12*, 165.
[29] J. Zou, F. Kim, *Nat. Commun.* **2014**, *5*, 5254.
[30] R. D. Deegan, O. Bakajin, T. F. Dupont, G. Huber, S. R. Nagel, T. A. Witten, *Nature* **1997**, *389*, 827.
[31] W. Sempels, R. D. Dier, H. Mizuno, J. Hofkens, J. Vermant, *Nat. Commun.* **2013**, *4*, 1757.
[32] I. I. Smalyukh, O. V. Zribi, J. C. Butler, O. D. Lavrentovich, G. C. L. Wong, *Phys. Rev. Lett.* **2006**, *96*, 177801.
[33] W. Han, M. Byun, B. Li, X. Pang, Z. Lin, *Angew. Chem. Int. Ed.* **2012**, *51*, 12588.
[34] T. Ming, X. Kou, H. Chen, T. Wang, H.-L. Tam, K.-W. Cheah, J.-Y. Chen, J. Wang, *Angew. Chem. Int. Ed.* **2008**, *47*, 9685.
[35] Z. Zhang, X. Zhang, Z. Xin, M. Deng, Y. Wen, Y. Song, *Adv. Mater.* **2013**, *25*, 6714.
[36] Y. Deng, X.-Y Zhu, T. Kienlen, A. Guo, *J. Am. Chem. Soc.* **2006**, *128*, 2768.
[37] Y. Kim, G. B. Hurst, M. J. Doktycz, M. V. Buchanan, *Anal. Chem.* **2001**, *73*, 2617.
[38] R. G. Larson, *Angew. Chem. Int. Ed.* **2012**, *51*, 2546.
[39] M. Anyfantakis, D. Baigl, *Angew. Chem. In. Ed.* **2014**, *53*, 14077.
[40] P. J. Yunker, T. Still, M. A. Lohr, A. G. Yodh, *Nature* **2011**, *476*, 308.
[41] T. Still, P. J. Yunker, A. G. Yodh, *Langmuir* **2012**, *28*, 4984.
[42] M. Anyfantakis, Z. Geng, M. Morel, S. Rudiuk, D. Baigl, *Langmuir* **2015**, *31*, 4113.
[43] A. Singh, R. D. Gunning, S. Ahmed, C. A. Barrett, N. J. English, J. Garate, K. M. Ryan, *J. Mater. Chem.* **2012**, *22*, 1562.
[44] M. Majumder, C. S. Rendall, J. A. Eukel, J. Y. L. Wang, N. Behabtu, C. L. Pint, T.-Y. Liu, A. W. Orbaek, F. Mirri, J. Nam, A. R. Barron, R. H. Hauge, H. K. Schmidt, M. Pasquali, *J. Phys. Chem. B* **2012**, *116*, 6536.
[45] M. Zanella, R. Gomes, M. Povia, C. Giannini, Y. Zhang, A. Riskin, M. V. Bael, Z. Hens, L. Manna, *Adv. Mater.* **2011**, *23*, 2205.
[46] R. M. Pasquarelli, D. S. Ginley, R. O'Hayre, *Chem. Soc. Rev.* **2011**, *40*, 5406.
[47] B. G. Prevo, O. D. Velev, *Langmuir* **2004**, *20*, 2099.
[48] Y. F. Li, Y. J. Sheng, H. K. Tsao, *Langmuir* **2013**, *29*, 7802.
[49] V. R. Dugyala, M. G. Basavaraj, *Langmuir* **2014**, *30*, 8680.
[50] J.-H. Wang, B. Wang, Q. Liu, Q. Li, H. Huang, L. Song, T.-Y. Sun, H. Wang, X.-F. Yu, C. Li, P. K. Chu, *Biomaterials* **2013**, *34*, 4274.
[51] H. B. Eral, J. M. Oh, *Colloid Polym. Sci.* **2013**, *291*, 247.

ADVANCED MATERIALS

Supporting Information

for *Adv. Mater.*, DOI: 10.1002/adma.201505617

Evaporative Self-Assembly of Gold Nanorods into Macroscopic 3D Plasmonic Superlattice Arrays

Penghui Li, Yong Li, Zhang-Kai Zhou, Siying Tang, Xue-Feng Yu, Shu Xiao, Zhongzhen Wu, Quanlan Xiao, Yuetao Zhao, Huaiyu Wang, and Paul K. Chu*

Supporting Information

Evaporative Self-Assembly of Gold Nanorods into Macroscopic Three-Dimensional Plasmonic Superlattice Arrays

Penghui Li, Yong Li, Zhang-Kai Zhou, Siying Tang, Xue-Feng Yu, Shu Xiao, Zhongzhen Wu, Quanlan Xiao, Yuetao Zhao, Huaiyu Wang, Paul K. Chu**

Dr. P. Li, Y. Li, S. Tang, Prof. X.-F. Yu, Dr. Q. Xiao, Dr. Y. Zhao, Prof. H. Wang
Institute of Biomedicine and Biotechnology, Shenzhen Institutes of Advanced Technology, Chinese Academy of Sciences, Shenzhen 518055, P. R. China.
E-mail: xf.yu@siat.ac.cn
Dr. P. Li, Prof. P. K. Chu
Department of Physics and Materials Science, City University of Hong Kong, Tat Chee Avenue, Kowloon, Hong Kong, P. R. China.
E-mail: paul.chu@cityu.edu.hk
Prof. Z.-K. Zhou
State Key Laboratory of Optoelectronic Materials and Technologies, School of Physics and Engineering, Sun Yat-sen (Zhongshan) University, Guangzhou 510275, P. R. China.
S. Xiao, Prof. Z. Wu
School of Advanced Materials, Peking University Shenzhen Graduate School, Shenzhen 518055, P. R. China.

Keywords: self-assembly, gold nanorods, plasmonics, three-dimensional superlattice, gold nanocrystals

Experimental Section

Materials: Chloroauric acid ($HAuCl_4 \cdot 4H_2O$, 99.99%), hexadecyltrimethylammonium bromide (CTAB, 97.0%), sodium borohydride ($NaBH_4$, 96%), silver nitrate ($AgNO_3$, 99.8%), L-ascorbic acid (AA, 99.7%), Malachite green (MG, 99%), and Rhodamine 6G (R6G, 99%) were obtained from Sinopharm Chemical Reagent Co. Ltd. (Shanghai, China) and (11-Mercaptoundecyl)hexa(ethylene glycol) (MUDOL, 90%) was purchased from Sigma-Aldrich Co. USA. All the chemicals were used as received without further purification. Millipore™ Milli-Q water (resistivity >18 MΩ cm^{-1} at 25 ^{o}C) was used in all the experiments. Silicon wafers (Si) with the <100> orientation were bought from Lijing Photoelectric Technology Co. Ltd. (Zhejiang, China).

Synthesis of AuNRs: The AuNRs were synthesized by the seed-mediated method in the CTAB solution as described previously. Briefly, 3-4 nm gold seed particles were prepared by mixing $HAuCl_4$ (0.5 mM, 5 mL) and CTAB (0.2 M, 5 mL). The solution was stirred vigorously followed by addition freshly prepared ice-cold $NaBH_4$ (10 mM, 600 µL). After vigorous stirring for 2 min, the seed solution was stored at room temperature for further use. In the AuNR synthesis, $HAuCl_4$ (5 mM, 18 mL) and $AgNO_3$ (0.1 M, 225 µL) were added to CTAB (0.2 M, 90 mL) and then HCl (1.2 M, 225 µL) and ascorbic acid (10 mM, 11.1 mL) were added and gently swirled as the color changed from dark orange to colorless. After the color change, the CTAB-stabilized gold seed solution (150 µL) was injected rapidly and the solution was gently mixed for 10 s and left undisturbed overnight. Finally, the solution was centrifuged at 12,000 rpm for 15 min to stop the reaction. The supernatant was removed and precipitate was resuspended in ultrapure water. The concentration of the final CTAB-AuNRs was estimated to be about 0.8 nM according to the extinction coefficient at the longitudinal SPR wavelength.

Surface ligand exchange of AuNRs: Freshly synthesized CTAB-AuNRs solution (5 mL) was purified by a second centrifugation step (10000 rpm, 10 min) to remove the excess CTAB. The precipitate was dispersed in Milli-Q water (5 mL) and mixed with MUDOL solution (0.2 mM, 5mL). The mixture was vortexed briefly and stirred gently at room temperature for 24 h to achieve saturated adsorption of MUDOL molecules on the AuNRs. The final MUDOL-AuNRs were condensed and used in the self-assembling experiments without further purification.

Self-assembly of AuNRs: A simple evaporative self-assembly process was utilized to prepare the 3D-superlattice arrays of AuNRs. The Si wafers were oxidized thermally to obtain a 300 nm thick surface oxide as the substrate. The MUDOL-AuNRs suspension was used as the suspension for evaporation onto the substrate. A drop of the AuNRs suspension (15.0 nM, 4.0 µL) was dripped onto the Si/SiO_2 substrate and the sessile droplet was kept stationary at

room temperature at a humidity of 85 ± 5% for up to 72 h to evaporate the water. The obtained 3D-superlattice arrays were cleaned by an oxygen plasma (60 s, 0.4 mbar, 100 W) and UV/ozone (1 h).

The other two kinds of arrays were prepared as the control. When CTAB-AuNRs were used to replace MUDOL-AuNRs as the suspension, coffee-ring arrays of AuNRs were obtained by the same procedures. On the other hand, when Si wafers were used to replace the Si/SiO_2 wafers as the substrate, few-layer arrays of AuNRs were obtained.

Characterizations: The absorption spectra were acquired on a Lambda 750 UV/VIS/NIR spectrometer (Perkin Elmer, USA) and FTIR spectra were obtained on a VERTEX 70 spectrometer (Bruker, Germany). The TEM images were taken on a JEOL-2010 transmission electron microscope (JEOL Ltd., Japan) at a voltage of 200 kV. The mean length and diameter of the AuNRs were determined from the corresponding size histograms using the open access ImageJ software. The zeta potential was determined on the Zetasizer Nano ZS (Malvern Instruments Ltd., UK) at 25 °C and the surface chemical structure was determined by X-ray photoelectron spectroscopy (XPS, PHI 5802, Physical Electronics, USA). The surface morphology and surface roughness were analyzed with an AFM (Multimode 8, Bruker, USA). The advancing and receding contact angles (θ_a and θ_r) were measured on the DSA25 contact angle goniometer and droplet shape analysis system (Kruss, Germany). The AuNRs suspension (4.0 μL) was dropped and removed dynamically and each contact angle value was the average of at least five independent measurements. The 3D images were obtained on a VK-X200 3D laser scanning confocal microscope (Keyence, Japan). The SEM images were acquired on a ZEISS SUPRA 55 (Carl Zeiss, Germany) field-emission scanning electron microscopy and cross-sectional examination was made on the cleaved samples.

Raman scattering experiments: The arrays were soaked in aqueous solutions overnight for adsorption of the MG molecules. Raman scattering was performed on a Horiba Jobin-Yvon LabRam HR VIS high-resolution confocal Raman microscope equipped with a 633 nm

laser as the excitation source at room temperature. The acquisition time for the measurement with MG 1.0×10^{-5} M was 1 s and that of MG at concentrations between 1.0×10^{-6} and 1.0×10^{-10} M was 10 s. The SERS intensity maps were obtained using the mapping software provided by the manufacturer from an area of 70 × 70 μm^2 using a step size of 5 µm (15 × 15 spots each) and acquisition time of 500 ms during laser excitation.

Characterization of the Si and Si/SiO_2 wafers

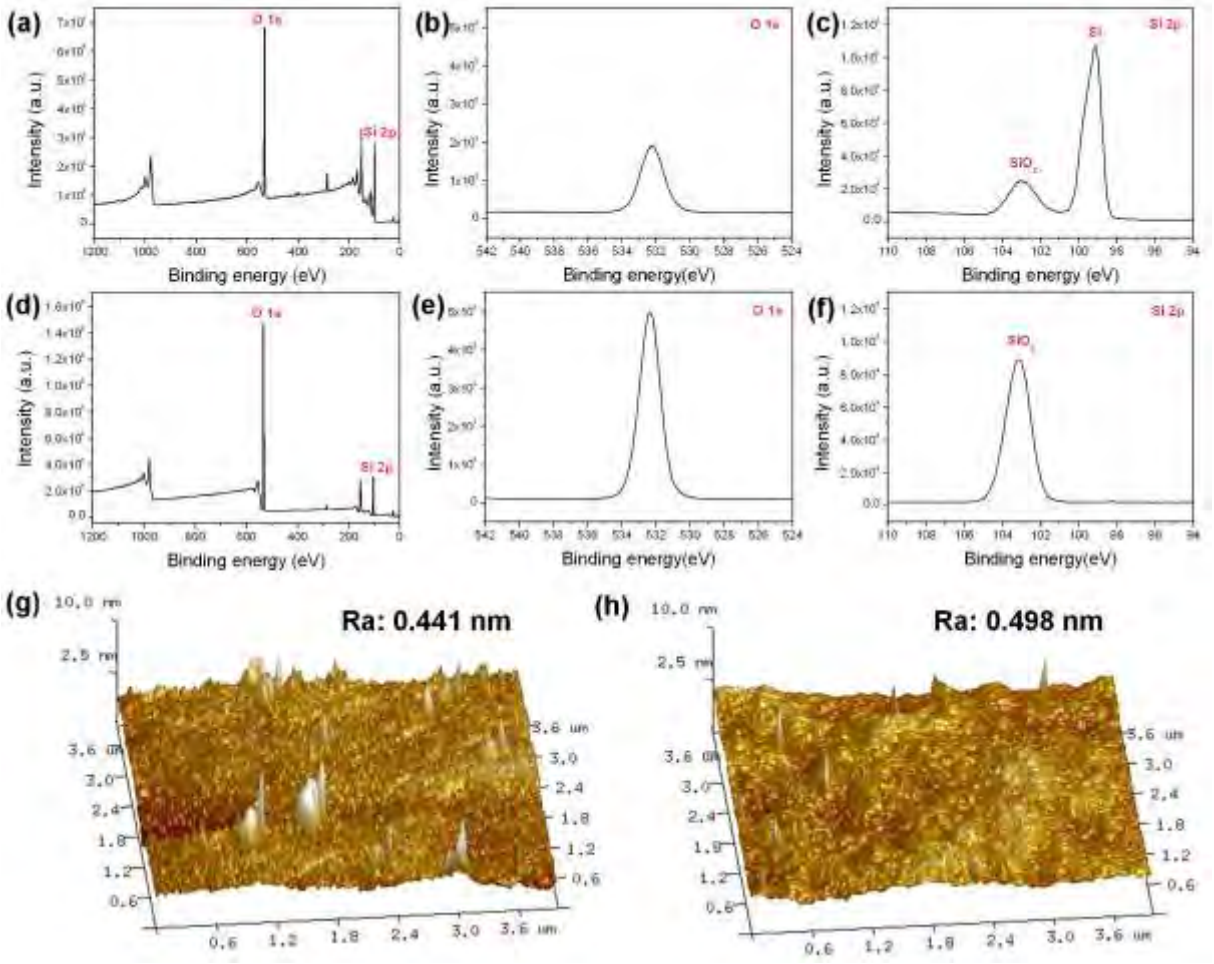

Figure S1. Surface survey XPS spectra, high-resolution O 1s spectra, and high-resolution Si 2p spectra of Si (a-c) and Si/SiO_2 (d-f), and AFM images with the value of Roughness Average (Ra) of Si (g) and Si/SiO_2 (h).

Measurement of contact angle hysteresis

Table S1. Advancing contact angle (θ_a), receding contact angle (θ_r), and contact angle hysteresis ($\Delta\theta$) of two AuNRs suspensions on the two substrates.

Liquid	Substrate	θ_a (degree)	θ_r (degree)	$\Delta\theta$ (degree)
CTAB-AuNRs	Si	51.0	18.2	32.8
	Si/SiO_2	46.6	14.2	32.4
MUDOL-AuNRs	Si	60.9	39.0	21.9
	Si/SiO_2	49.1	38.0	11.1

Deposition behavior of the CTAB-AuNRs on Si during evaporation

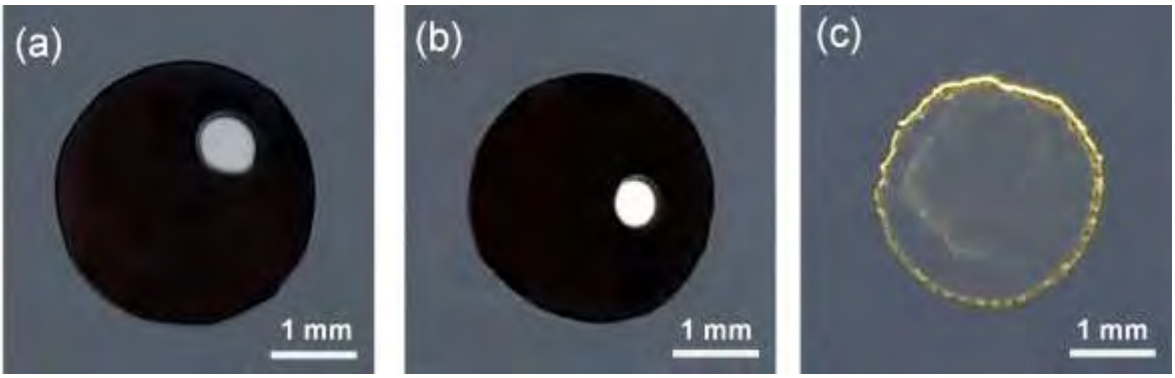

Figure S2. Top-view of CTAB-AuNRs deposition during evaporation on Si.

Assembly formed by CTAB-AuNRs within MUDOL suspension evaporated on Si/SiO_2

Droplets of CTAB-AuNRs with added MUDOL (without the ligand exchange protocol) are evaporated on the Si/SiO_2 substrate. The inset photograph of Figure S3a demonstrates that the coffee-ring effect can also be avoided and the disk-like stain is formed. However, the SEM observation shows that the stain is formed with loosely dispersed assembled clusters (Figure S3a), and only partial of the AuNRs exhibit the vertically aligned structure within the assembly (Figure S3b). The results demonstrate that without the ligand exchange protocol, the totally reverse of the coffee-ring and the perfect ordered assembly of AuNRs cannot be achieved, despite the partially ligand exchange reaction of CTAB-AuNRs within the MUDOL suspension during the evaporation.

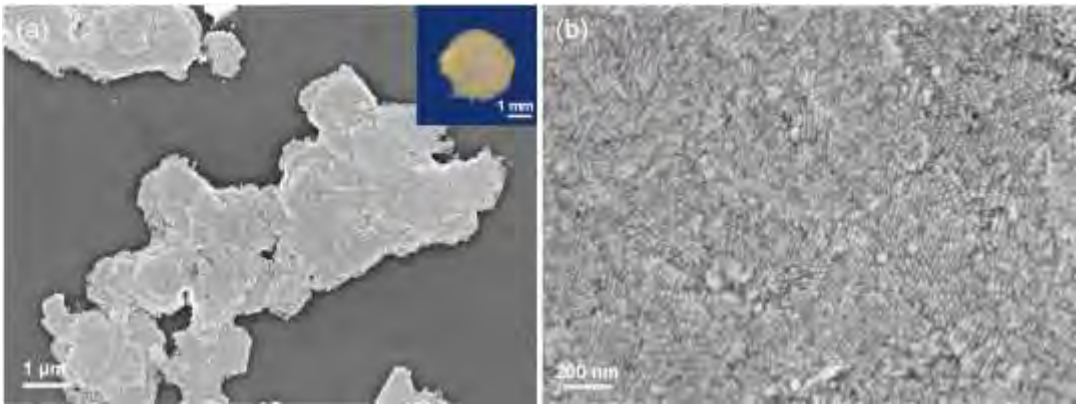

Figure S3. SEM images with inset photograph of assembly formed by CTAB-AuNRs within the MUDOL suspension evaporated on Si/SiO_2.

SERS performance of the coffee-ring array

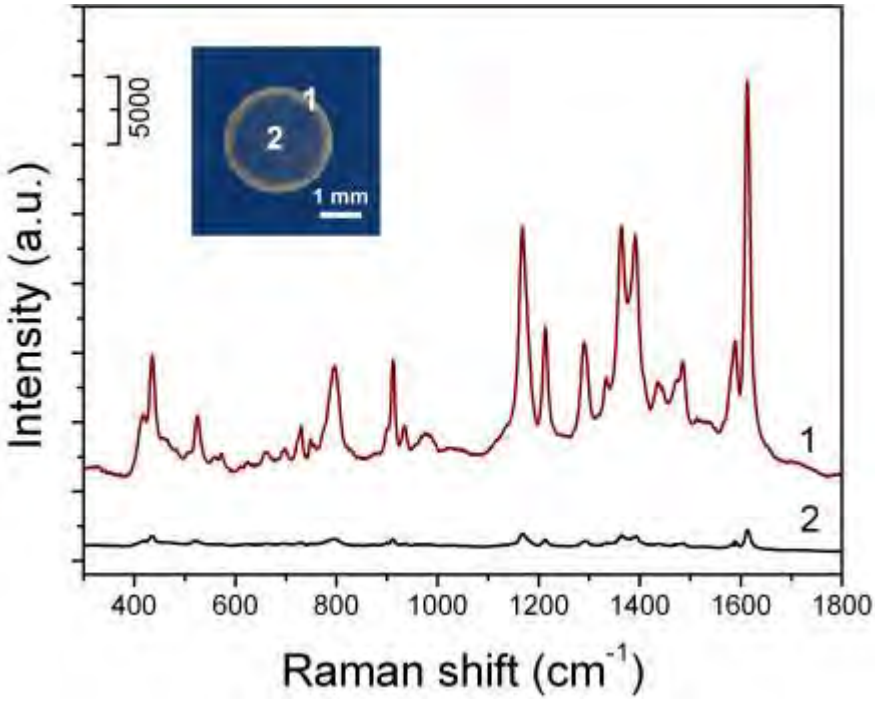

Figure S4. Typical SERS spectra (λ_{ex} = 633 nm) of MG (1.0×10^{-5} M) acquired from the outer rim (area 1) and middle area (area 2) of coffee-ring array.

Numerical calculations

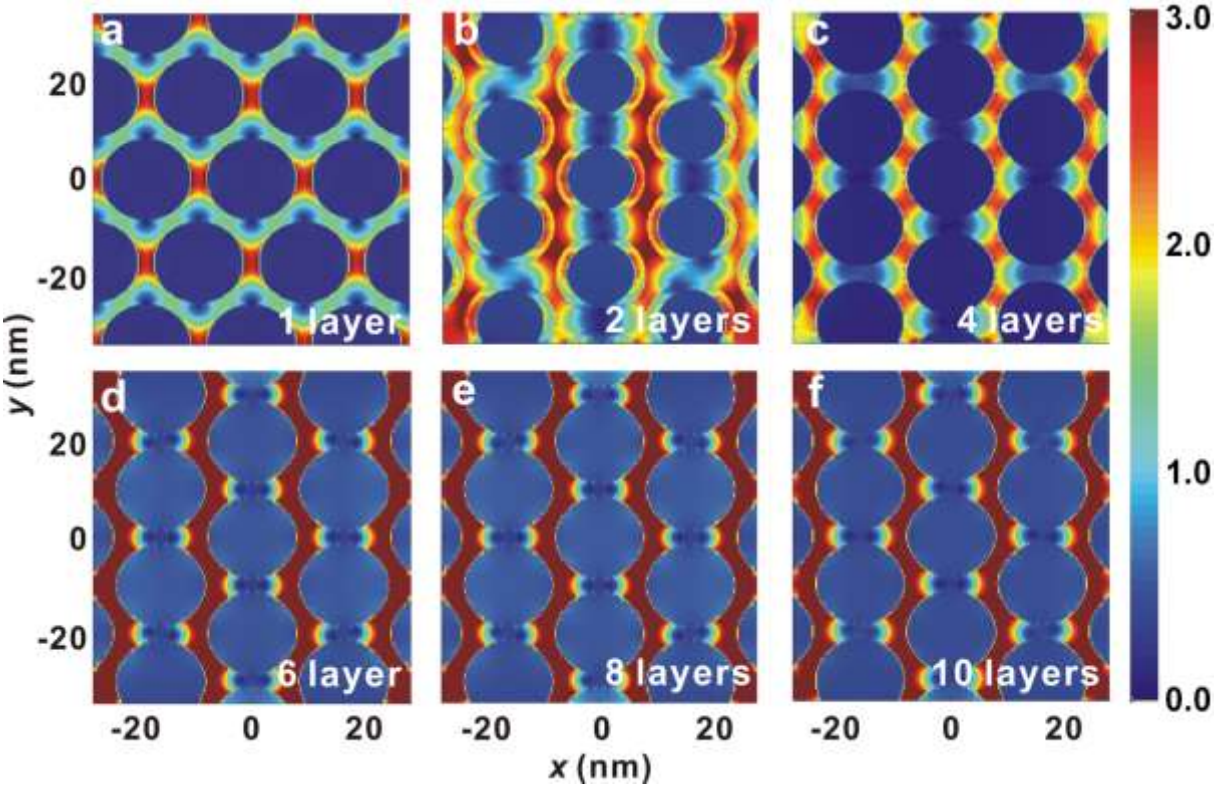

Figure S5. Field distributions of AuNRs arrays with layer numbers of 1, 2, 4, 6, 8, and 10, in which the AuNRs are vertically aligned with respect to the surface of the substrate. A plane wave is applied as the excitation source and the results are acquired at a wavelength of 633 nm from the plane 3.95 nm under the surface. The electric field intensity enhancement of the AuNRs arrays is evaluated by the finite-difference time-domain (FDTD) method (FDTD Solutions 8.0, Lumerical Solutions, Inc.). The calculation model comprises layers of the AuNRs arrays with ordered honeycomb-like lattice cells. A single nanorod is formed by a cylinder with two ellipsoids on the two ends. The length and diameter of the cylinder are set to be 58.0 and 16.3 nm whereas the long and short radii of the ellipsoid are 8.15 and 3.95, respectively. The center-to-center distance of two adjacent nanorods is 19.2 nm. The complex dielectric constants of Au are taken from the paper of Johnson and Christy.[1] In the calculation, we use periodic boundary conditions in the x–y plane and perfectly matched layers (PMLs) in the z direction. The unit cell is taken as 57.6 nm × 66.51 × 3000 nm. Comparison of the simulation results from arrays with different layers indicates that a larger layer number leads to more homogeneous and stronger near-field localization in the gaps of the AuNRs to enhance the SERS response. These nanoscale gaps in the nanorod forest can trap liquids due to the capillary force[2,3] and this is another advantage of the vertically aligned AuNRs arrays in sensing applications.

[1] P. B. Johnson, R. W. Christy, *Phys. Rev. B* **1972,** 6, 4370.
[2] J. Bico, U. Thiele, D. Quéré, *Colloids Surf. A* **2002,** 206, 41.
[3] L. Wang, Y. Zhao, J. Wang, X. Hong, J. Zhai, L. Jiang, F. Wang, *Appl. Surf. Sci.* **2009,** 255, 4944.